Postselection-free controlled generation of high dimensional OAM entangled state

Suman Karan,* Radhika Prasad, and Anand K. Jha

Department of Physics, Indian Institute of Technology Kanpur, Kanpur, UP 208016, India

arXiv:2203.14799v1 [quant-ph] 28 Mar 2022

Abstract

High-dimensional entangled states in orbital angular momentum (OAM) basis offer unique advantages for several quantum information applications. However, a given quantum information application for its optimal performance requires generation of a specific OAM entangled state with full control over the shape of the OAM Schmidt spectrum. Spontaneous parametric down-conversion (SPDC) is the most widely used method for generating OAM entangled states. Most of the existing methods for controlling the generation of the state employ postselection, which invariably compromises the security benefits of quantum information applications. The postselection-free generation of OAM entangled states can be achieved either by adjusting the SPDC phase matching condition or by shaping the profile of the pump field used for down-conversion. While it is known that the phase matching adjustments can only change the width of the OAM Schmidt spectrum, even the most recent works based on pump shaping have demonstrated generation of only up to 24-dimensional states with very limited control over the OAM Schmidt spectrum. Here, we propose and experimentally demonstrate a technique that employs both the phase matching adjustments and pump-shaping for generating high-dimensional OAM entangled states with complete control over the shape of the OAM Schmidt spectrum. We report generation of up to 200-dimensional OAM entangled states with three different spectra, namely, Gaussian, rectangular and triangular, with up to 99% generation accuracy.

I. INTRODUCTION

A Laguerre-Gaussian (LG) mode $LG_p^l(\rho, \phi)$ is characterized by two indices l and p, where l is referred to as the orbital angular momentum (OAM) mode index and p is referred to as the radial mode index. A photon in an LG mode with the OAM mode index of l carries OAM of $l\hbar$ [1]. The OAM of a photon provides a discrete infinite-dimensional basis [2] as opposed to the two-dimensional polarization basis [3]. The use of high-dimensional entangled states provides higher security against eavesdropper attacks in entanglement-enabled quantum cryptographic schemes [4–6], increased information capacity [7, 8], enhanced robustness of communication protocols in noisy environment [9, 10], and stronger violations

* sumankaran2@gmail.com

of generalized Bell's inequalities [11–13]. High-dimensional entangled states also have important implications for dense coding [14, 15], quantum teleportation [16–18], entanglement swapping [19, 20], and supersensitive measurements [21–23]. The most widely used process for generating entangled photon pairs in the OAM basis is spontaneous parametric down-conversion (SPDC) [24, 25]. It is a nonlinear optical process in which a pump photon of higher frequency splits into two photons of lower frequencies, called the signal and idler. SPDC process conserves OAM as $l_p = l_s + l_i$ where p, s and i denote pump, signal and idler, and l_p, l_s and l_i are the OAM mode indices of the pump, signal, and idler photons, respectively [25]. For the pump field with OAM mode index, $l_p = 0$, the generated entangled photon pair follows Schmidt decomposition and the two-photon state in the OAM basis can be written as $|\psi\rangle_{tp} = \sum_l \sqrt{S_l}|l\rangle_s|-l\rangle_i$. Here, S_l is the probability of detecting signal and idler photons with OAM of $l\hbar$ and $-l\hbar$, respectively and is called the two-photon OAM Schmidt spectrum [26].

For the optimal performance of any quantum information application, one requires generation of OAM entangled states with complete control over the OAM Schmidt spectrum S_l. For instance, applications in quantum teleportation [27] and quantum key distribution [28–30] need rectangular OAM Schmidt spectra. So far, postselection techniques such as procrustean filtering are utilized for controlling the generation of OAM entangled states [31]. However, such postselected states compromise the security benefits of quantum information protocols [13, 32, 33]. The existing techniques for postselection-free generation of OAM entangled states involve either tuning the phase matching of the SPDC process [34–36] or shaping the profile of the pump field [26, 37, 38]. However, tuning the phase matching only changes the width of the OAM Schmidt spectrum [34–36] and even the most recent works based on shaping of the pump profile have demonstrated generation of only up to 24-dimensional states with very limited control over the OAM Schmidt spectrum [39–41].

In contrast, in this paper, we propose and experimentally demonstrate a technique that employs both the phase matching adjustments and pump-shaping for generating high-dimensional OAM entangled states with complete control over the shape of the OAM Schmidt spectrum. Figure 1(a) illustrates the OAM Schmidt spectrum obtained with a Gaussian pump ($LG_{p=0}^{l_p=0}$) and collinear phase matching. Figure 1(b) describes our technique. We use non-collinear phase matching for the SPDC, and for the pump field, we use coherent superposition of Laguerre-Gaussian (LG) radial modes with OAM mode index

$l_p = 0$.

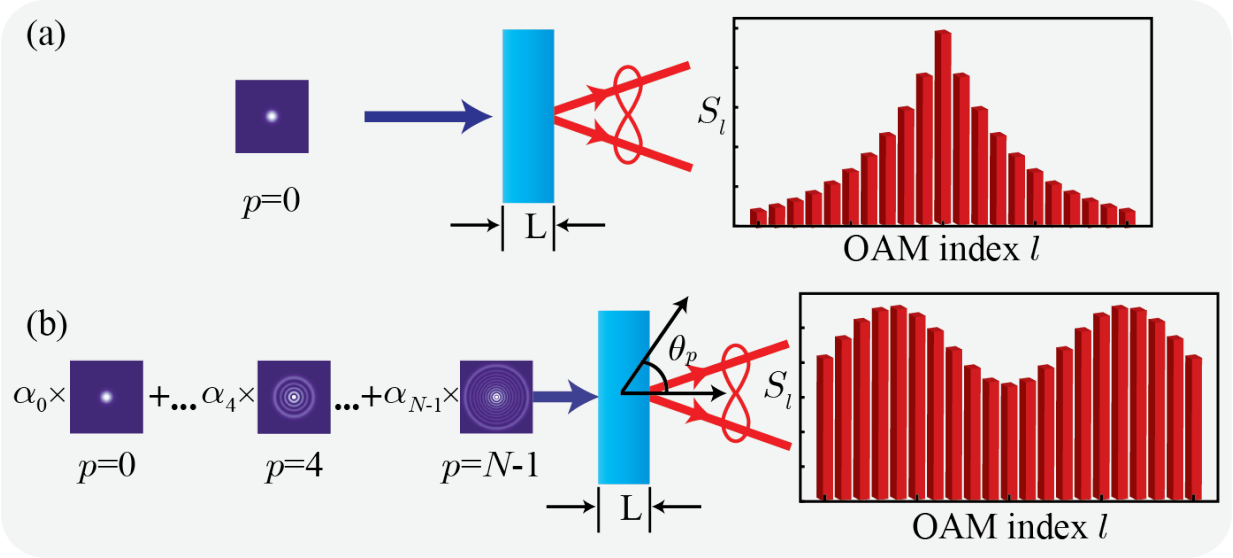

FIG. 1. (a) Schematic representation of the generation of the OAM Schmidt spectrum from a Gaussian pump ($LG_{p=0}^{l_p=0}$) with collinear phase matching. (b) Schematic representation of the postselection-free controlled generation of OAM spectra employing non-collinear phase matching and the pump field shaping.

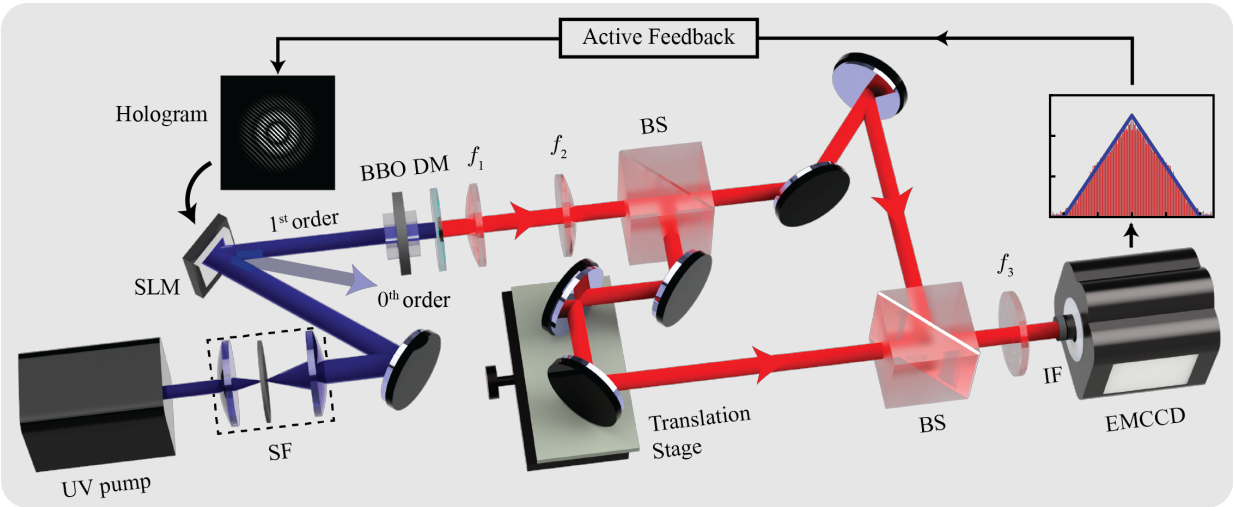

FIG. 2. Schematic of the experimental setup. SF: spatial filter, SLM: spatial light modulator, BBO: β- barium borate crystal, DM: dichroic mirror, BS: 50:50 non-polarization beam splitter, IF: interference filter of central wavelength 810 and 10 nm bandwidth.

II. THEORY

The two-photon state generated by type-I SPDC in the transverse momentum basis can be written as [37, 42–44]

$$|\psi_{\rm tp}\rangle = \iint V(\mathbf{q}_s, \mathbf{q}_i)\Phi(\mathbf{q}_s, \mathbf{q}_i)|\mathbf{q}_s\rangle_s|\mathbf{q}_i\rangle_i d^2\mathbf{q}_s d^2\mathbf{q}_i, \tag{1}$$

where $|\mathbf{q}_s\rangle_s$, $|\mathbf{q}_i\rangle_i$ are the signal and idler state vectors in transverse momentum basis, respectively. $V(\mathbf{q}_s, \mathbf{q}_i)$ is the pump amplitude and $\Phi(\mathbf{q}_s, \mathbf{q}_i)$ is the phase matching function. We express the above two-photon state in the Laguerre-Gaussian (LG) basis as

$$|\psi_{\rm tp}\rangle = \sum_{l_s,p_s}\sum_{l_i,p_i} C_{l_i,p_i}^{l_s,p_s}|l_s, p_s\rangle_s|l_i, p_i\rangle_i. \tag{2}$$

Here $|l_s, p_s\rangle_s$ is the state vector corresponding to the signal photon, etc. Using Eqs. (1) and (2), the two-photon complex coefficient $C_{l_i,p_i}^{l_s,p_s}$ can be written as [38, 45]

$$C_{l_i,p_i}^{l_s,p_s} = A\iint d^2\boldsymbol{q}_s d^2\boldsymbol{q}_i V(\boldsymbol{q}_s, \boldsymbol{q}_i)\Phi(\boldsymbol{q}_s, \boldsymbol{q}_i)\left[LG_{p_s}^{l_s}(\boldsymbol{q}_s)\right]^*\left[LG_{p_i}^{l_i}(\boldsymbol{q}_i)\right]^*, \tag{3}$$

where $LG_p^l(\boldsymbol{q}) = \langle \boldsymbol{q}|l, p\rangle$ is the momentum basis representation of the LG mode [37]. Now, transforming into cylindrical polar coordinates in the transverse momentum basis, we write $C_{l_i,p_i}^{l_s,p_s}$ as

$$C_{l_i,p_i}^{l_s,p_s} = \int_0^\infty\int_{-\pi}^{\pi} V(\rho_s, \rho_i, \phi_s, \phi_i)\Phi(\rho_s, \rho_i, \phi_s, \phi_i)\left[LG_{p_s}^{l_s}(\rho_s, \phi_s)\right]^*\left[LG_{p_i}^{l_i}(\rho_i, \phi_i)\right]^*\rho_s\rho_i d\rho_s d\rho_i d\phi_s d\phi_i. \tag{4}$$

Here $\boldsymbol{q}_s = (q_{sx}, q_{sy}) = (\rho_s\cos\phi_s, \rho_s\sin\phi_s)$, $\boldsymbol{q}_i = (q_{ix}, q_{iy}) = (\rho_i\cos\phi_i, \rho_i\sin\phi_i)$, $d\boldsymbol{q}_s = \rho_s d\rho_s d\phi_s$, and $d\boldsymbol{q}_i = \rho_i d\rho_i d\phi_i$. $P_{l_i}^{l_s}$ is the probability of detecting the signal and idler photons with OAM $l_s\hbar$ and $l_i\hbar$, and it can be written as a summation over the radial modes

$$P_{l_i}^{l_s} = \sum_{p_s=0}^{\infty}\sum_{p_i=0}^{\infty}|C_{l_i,p_i}^{l_s,p_s}|^2. \tag{5}$$

When $l_p = 0$, conservation of OAM leads to $l_s = -l_i = l$ [25], and in this case, Eq. (2) takes the following Schmidt decomposed form:

$$|\psi\rangle_{tp} = \sum_l \sqrt{S_l}|l\rangle_s|-l\rangle_i. \tag{6}$$

Here $S_l = P^l_{-l}$ is called the OAM Schmidt spectrum. Using Eqs. (4) and (5), and employing the identity $\sum_{p=0}^{\infty}(LG)^l_p(\rho)(LG)^{*l}_p(\rho') = \frac{1}{\pi}\delta(\rho^2 - \rho'^2)$ [21], we write S_l as

$$S_l = \frac{1}{4\pi^2}\iint_0^{\infty}\rho_s\rho_i\left|\iint_{-\pi}^{\pi}V(\rho_s,\rho_i,\phi_s,\phi_i)\Phi(\rho_s,\rho_i,\phi_s,\phi_i)e^{-il(\phi_s-\phi_i)}d\phi_s d\phi_i\right|^2 d\rho_s d\rho_i. \tag{7}$$

We express the pump amplitude $V(\rho_s,\rho_i,\phi_s,\phi_i)$ as a coherent superposition of the radial modes

$$V(\rho_s,\rho_i,\phi_s,\phi_i) = \sum_{p=0}^{N-1}\alpha_p LG_p^{l_p=0}(\rho_s,\rho_i,\phi_s,\phi_i), \tag{8}$$

where α_p is the complex coefficient and N is the total number of radial modes in the superposition. The amplitude $LG_p^{l_p=0}(\rho_s,\rho_i,\phi_s,\phi_i)$ can be written as [46]

$$LG_p^{l_p=0}(\rho_s,\rho_i,\phi_s,\phi_i) = \left[\frac{w}{2\pi}\right]^{\frac{1}{2}} L_p^0\left[\frac{w^2\rho_p^2}{2}\right]\exp\left[-\frac{w^2\rho_p^2}{4}\right]\exp\left[i\pi p\right]. \tag{9}$$

Here L_p^0 is the associated Laguerre polynomial, $\rho_p^2 = \rho_s^2 + \rho_i^2 + 2\rho_s\rho_i\cos(\phi_s - \phi_i)$, and w is the beam waist of the pump field. Now, we write the phase matching function $\Phi(\rho_s,\rho_i,\phi_s,\phi_i)$ of Eq. (7) as [36, 42, 43]

$$\Phi(\rho_s,\rho_i,\phi_s,\phi_i) = \mathrm{sinc}\left(\frac{\Delta k_z L}{2}\right)\exp\left[i\frac{\Delta k_z L}{2}\right], \tag{10}$$

where L is the thickness of the crystal and Δk_z is called the phase mismatch parameter. Δk_z can be tuned by changing the phase matching angle θ_p, which is the angle between the propagation direction of the pump field and the optic axis of the nonlinear crystal. For the detailed expression of Δk_z, see Supplementary Information Sec. I. We note that for a given N, non-collinear phase matching conditions allow the generation of much larger variety of OAM spectra than the collinear phase matching condition. So, in our scheme, we generate a given OAM spectrum by optimizing the phase matching angle θ_p and the complex coefficients α_p.

For optimization, in the case of a $2D+1$ dimensional spectrum, we define the normalized mean square error ΔE as [47]

$$\Delta E = \frac{\sum_{l=-D}^{+D}\left(S_l^{\mathrm{e}} - S_l^{\mathrm{o}}\right)^2}{\sum_{l=-D}^{+D}\left(S_l^{\mathrm{e}} - \langle S_l^{\mathrm{e}}\rangle\right)^2}\times 100\%, \tag{11}$$

where S_l^{e} and S_l^{o} are the expected and obtained OAM Schmidt spectra, and $\langle S_l^{\mathrm{e}}\rangle$ is the mean of S_l^{e}. ΔE is minimized by optimizing both the complex coefficients α_p and the phase

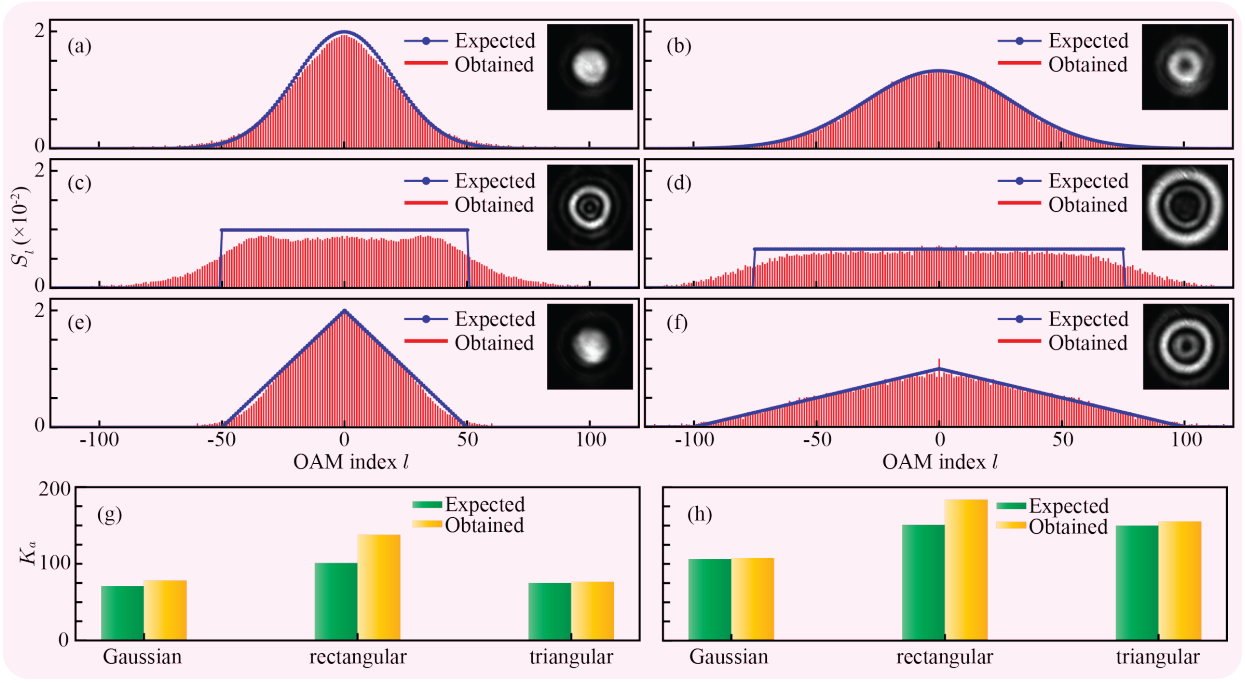

FIG. 3. Experimentally generated OAM Schmidt spectrum with $L = 5$ mm, and $\theta_p = 28.69°$. The pump field is in the form of a coherent superposition of five radial modes having $p = 0$ to $p = 4$ with OAM index $l_p = 0$. (a), (b) Expected and experimentally obtained OAM Schmidt spectra of Gaussian shape with two different widths. (c), (d) Expected and experimentally obtained OAM Schmidt spectra of rectangular shape with two different widths. (e), (f) Expected and experimentally obtained OAM Schmidt spectra of triangular shape with two different widths. (g), (h) Expected and experimentally obtained angular Schmidt number K_a for the different spectra with two different widths shown above.

matching angle θ_p. Using Eq. (7), we calculate S_l, and obtain the coefficients numerically using a particle swarm optimization technique for the desired spectrum [48]. The optimization is carried out with the help of the Python package called 'pyswarm'. These numerically determined coefficients serve as the starting point for the experimental implementation. In our experiments, for measuring the OAM Schmidt spectrum, we use an interferometric technique as described in Ref. [49]. As described in Ref. [36], the OAM Schmidt spectrum S_l remains the same as the OAM spectrum of either the signal or the idler photon. Therefore, for measuring the OAM Schmidt spectrum, we need to make measurements on only the signal or the idler photon.

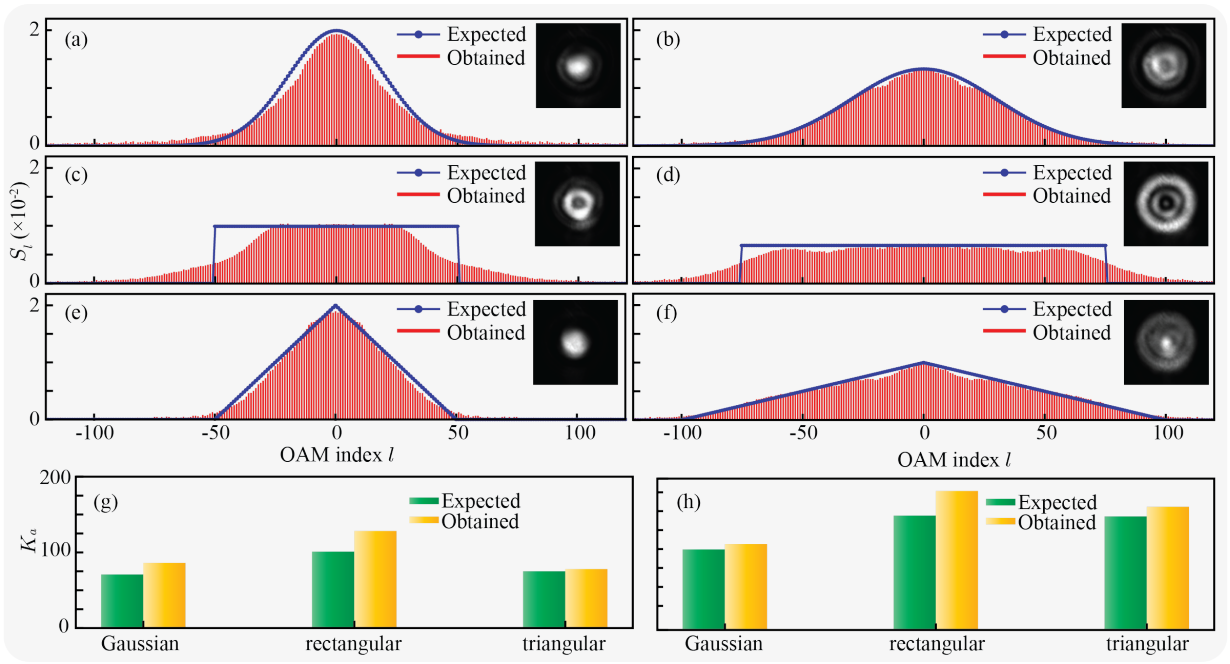

FIG. 4. Experimentally generated OAM Schmidt spectrum with $L = 15$ mm, and $\theta_p = 28.71°$. The pump field is in the form of a coherent superposition of five radial modes having $p = 0$ to $p = 4$ with OAM index $l_p = 0$. (a), (b) Expected and experimentally obtained OAM Schmidt spectra of Gaussian shape with two different widths. (c), (d) Expected and experimentally obtained OAM Schmidt spectra of rectangular shape with two different widths. (e), (f) Expected and experimentally obtained OAM Schmidt spectra of triangular shape with two different widths. (g), (h) Expected and experimentally obtained angular Schmidt number K_a for the different spectra with two different widths shown above.

III. EXPERIMENTS

The experimental setup is depicted in Fig. 2. We use a 100 mW TOPTICA TopMode ultraviolet (UV) continuous wave (CW) laser of wavelength $\lambda_p = 405$ nm that is spatially filtered and incident on a HOLOEYE PLUTO-2-UV-099 spatial light modulator (SLM). The SLM is used for generating the pump in the form of a superposition of five radial modes using the method described by Arrizon et al. [50]. For the superposition, we use radial modes from $p = 0$ to $p = 4$ having beam waist $w = 320$ μm. This pump field is made incident on a β-barium borate (BBO) crystal of transverse dimensions 5 mm $\times$ 5 mm and thickness L. The crystal is kept on a goniometer to change the phase matching angle θ_p. A Dichroic mirror

(DM) is positioned just after the crystal to block UV while allowing the down-converted photon pairs to pass through. These photon pairs are incident on a Mach-Zehnder type interferometer [49], and the interferogram output is captured using an Andor iXon Ultra-897 electron-multiplied charged coupled device (EMCCD) camera with 512×512 pixel grids having pixel pitch of 16×16 μm^2. Lenses with focal lengths $f_1 = 50$ mm, and $f_2 = 200$ mm are placed in a $4f$ configuration to image the crystal plane with a magnification of four. The Fourier transform of this image plane is obtained at the camera plane using another lens of focal length $f_3 = 300$ mm. For capturing the interferograms, the camera acquisition time is kept in the range of $20 - 40$ seconds. An interference filter (IF) of central wavelength 810 nm and bandwidth 10 nm is placed in front of the camera. We experimentally measure the generated OAM Schmidt spectrum using the technique described in Ref. [49], and we refer to it as the obtained OAM Schmidt spectrum S_l^o. For the expected OAM Schmidt spectrum S_l^e, that we want to generate, we calculate the error ΔE. We optimize θ_p and α_p, measure the generated spectrum, and calculate ΔE until it reaches a minimum value $\Delta E_{\min}$.

Figure 3 presents the experimentally generated OAM spectra with a BBO crystal of $L = 5$ mm and $\theta_p = 28.69°$. Figures 3(a) and 3(b) illustrate the expected and experimentally obtained Gaussian OAM Schmidt spectra of two different widths characterized by standard deviations 20 and 30, respectively. Similarly, rectangular spectrum of widths 100 and 150 are shown in Figs. 3(c) and 3(d), respectively. Figures 3(e) and 3(f) are the triangular OAM Schmidt spectra of widths 100 and 200. The associated pump intensity profiles for generating each spectrum are shown as insets. Schmidt number is a way of characterizing the dimensionality of the Schmidt spectrum and is calculated using the formula $K_a = 1/\sum_l S_l^2$ [26, 51, 52]. Figures 3(g) and 3(h) show the expected and experimentally obtained angular Schmidt numbers K_a for the two different sets of Schmidt spectra. In order to demonstrate the versatility of our technique, we generate the same set of OAM Schmidt spectra, as shown in Fig. 3, using a crystal of thickness $L = 15$ mm. We find that in this case, the optimal value of $\theta_p = 28.71°$. The corresponding results are reported in Fig. 4. The superposition coefficients α_p for the spectra presented in the Figs. 3 and 4 are reported in the Supplementary Information Sec. II.

Although the Schmidt number characterizes the dimensionality of the spectrum, it does not capture the experimental accuracy of generating a spectrum. We, therefore, characterize the generation accuracy F of our scheme as $(100 - \Delta E_{\min})\%$ (see Eq. 11). The generation

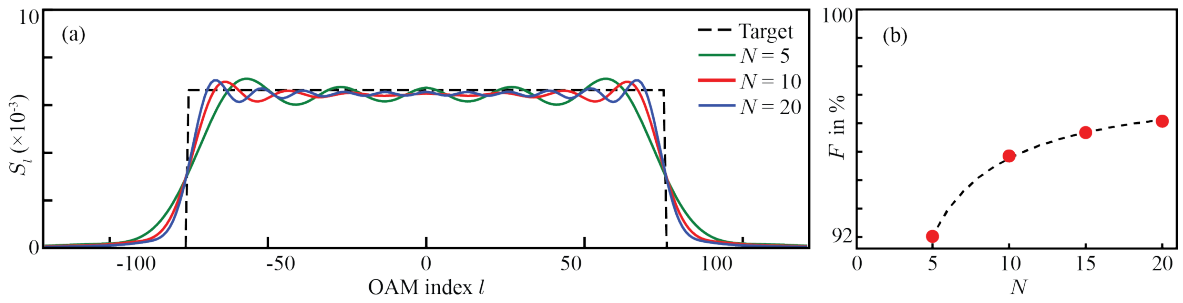

FIG. 5. (a) The simulation results for a rectangular spectrum generated with $N = 5$, 10 and 20. (b) Simulated generation accuracy (F) for different N. The dashed line denotes the best fit.

accuracy F for the spectra shown in Figs. 3 and 4 are presented in Table I. We note that for

TABLE I. Generation accuracy F for experimentally generated spectra reported in Figs. 3 and 4

Shape	Width	F in %	
		$L = 5$mm	$L = 15$mm
Gaussian	20	99.38	97.19
	30	99.80	99.39
rectangular	100	84.75	79.44
	150	80.63	84.03
triangular	100	99.55	99.12
	200	98.66	98.21

the Gaussian and triangular spectra, our generation accuracy F is more than 97%. However, for the rectangular spectra, F is around 80%. This is because, although the optimization using just the five radial modes is sufficient for the Gaussian and triangular spectra, one needs more radial modes to optimize for the rectangular spectrum. Next, we numerically investigate how increasing the number of radial modes improves the generation accuracy. For our numerical simulations, we keep $L = 15$ mm and $\theta_p = 28.71°$ and the rectangular spectrum of width 150 as our target (see Fig. 5). Figure 5(a) shows the results for $N = 5$, 10 and 20. In Fig. 5(b), we plot the generation accuracy F as a function of the total number of radial modes N. We see that as N increases the generation accuracy F also increases, and with $N = 20$, the generation accuracy F becomes more than 96%. The transverse dimension of our nonlinear crystal is 5 mm × 5 mm, with which it is not possible to fit an LG mode

of beam waist $w = 320$ μm with $p > 4$. However, in our numerical simulations, we find that with a nonlinear crystal of transverse dimensions 10 mm $\times$ 10 mm, one can fit very easily more than 20 radial modes and thereby achieve more than 96% generation accuracy.

IV. CONCLUSION

In conclusion, we have proposed and demonstrated an experimental technique for postselection-free controlled generation of OAM entangled states by SPDC. Our technique involves adjusting the SPDC phase matching and shaping the profile of the pump field for generating high-dimensional OAM entangled states with complete control over the shape of the OAM Schmidt spectrum. We have reported generation of up to 200-dimensional OAM entangled states with three different spectra, namely, Gaussian, rectangular and triangular, with up to 99% generation accuracy. Our work can have important implications for harnessing the full benefits of high-dimensional quantum information applications while ensuring the complete security benefits.

V. ACKNOWLEDGMENTS

We thank Girish Kulkarni for helpful discussions. We acknowledge financial support from the Science and Engineering Research Board (Grant No. STR/2021/000035) and from the Department of Science & Technology, Government of India (Grant No. DST/ICPS/QuST/Theme-1/2019). SK thanks the University Grant Commission (UGC), Government of India for financial support.

---

[1] L. Allen, M. W. Beijersbergen, R. J. C. Spreeuw, and J. P. Woerdman, Orbital angular momentum of light and the transformation of laguerre-gaussian laser modes, Physical Review A **45**, 8185 (1992).

[2] A. M. Yao and M. J. Padgett, Orbital angular momentum: origins, behavior and applications, Advances in Optics and Photonics **3**, 161 (2011).

[3] A. Forbes and I. Nape, Quantum mechanics with patterns of light: Progress in high dimensional and multidimensional entanglement with structured light, AVS Quantum Science **1**, 011701 (2019).

[4] H. Bechmann-Pasquinucci and A. Peres, Quantum cryptography with 3-state systems, Physical Review Letters **85**, 3313 (2000).

[5] G. M. Nikolopoulos, K. S. Ranade, and G. Alber, Error tolerance of two-basis quantum-key-distribution protocols using qudits and two-way classical communication, Physical Review A **73**, 032325 (2006).

[6] N. J. Cerf, M. Bourennane, A. Karlsson, and N. Gisin, Security of quantum key distribution usingd-level systems, Physical Review Letters **88**, 127902 (2002).

[7] J. Wang, J.-Y. Yang, I. M. Fazal, N. Ahmed, Y. Yan, H. Huang, Y. Ren, Y. Yue, S. Dolinar, M. Tur, and A. E. Willner, Terabit free-space data transmission employing orbital angular momentum multiplexing, Nature Photonics **6**, 488 (2012).

[8] N. Bozinovic, Y. Yue, Y. Ren, M. Tur, P. Kristensen, H. Huang, A. E. Willner, and S. Ramachandran, Terabit-scale orbital angular momentum mode division multiplexing in fibers, Science **340**, 1545 (2013).

[9] S. Ecker, F. Bouchard, L. Bulla, F. Brandt, O. Kohout, F. Steinlechner, R. Fickler, M. Malik, Y. Guryanova, R. Ursin, and M. Huber, Overcoming noise in entanglement distribution, Physical Review X **9**, 041042 (2019).

[10] F. Zhu, M. Tyler, N. H. Valencia, M. Malik, and J. Leach, Is high-dimensional photonic entanglement robust to noise?, AVS Quantum Science **3**, 011401 (2021).

[11] D. Collins, N. Gisin, N. Linden, S. Massar, and S. Popescu, Bell inequalities for arbitrarily high-dimensional systems, Physical Review Letters **88**, 040404 (2002).

[12] J. Leach, B. Jack, J. Romero, M. Ritsch-Marte, R. W. Boyd, A. K. Jha, S. M. Barnett, S. Franke-Arnold, and M. J. Padgett, Violation of a bell inequality in two-dimensional orbital angular momentum state-spaces, Optics Express **17**, 8287 (2009).

[13] A. C. Dada, J. Leach, G. S. Buller, M. J. Padgett, and E. Andersson, Experimental high-dimensional two-photon entanglement and violations of generalized bell inequalities, Nature Physics **7**, 677 (2011).

[14] F. Wang, M. Erhard, A. Babazadeh, M. Malik, M. Krenn, and A. Zeilinger, Generation of the complete four-dimensional bell basis, Optica **4**, 1462 (2017).

[15] X.-M. Hu, Y. Guo, B.-H. Liu, Y.-F. Huang, C.-F. Li, and G.-C. Guo, Beating the channel capacity limit for superdense coding with entangled ququarts, Science Advances **4**, 10.1126/sciadv.aat9304 (2018).

[16] Y.-H. Luo, H.-S. Zhong, M. Erhard, X.-L. Wang, L.-C. Peng, M. Krenn, X. Jiang, L. Li, N.-L. Liu, C.-Y. Lu, A. Zeilinger, and J.-W. Pan, Quantum teleportation in high dimensions, Physical Review Letters **123**, 070505 (2019).

[17] X.-L. Wang, X.-D. Cai, Z.-E. Su, M.-C. Chen, D. Wu, L. Li, N.-L. Liu, C.-Y. Lu, and J.-W. Pan, Quantum teleportation of multiple degrees of freedom of a single photon, Nature **518**, 516 (2015).

[18] X.-M. Hu, C. Zhang, B.-H. Liu, Y. Cai, X.-J. Ye, Y. Guo, W.-B. Xing, C.-X. Huang, Y.-F. Huang, C.-F. Li, and G.-C. Guo, Experimental high-dimensional quantum teleportation, Physical Review Letters **125**, 230501 (2020).

[19] Y. Zhang, M. Agnew, T. Roger, F. S. Roux, T. Konrad, D. Faccio, J. Leach, and A. Forbes, Simultaneous entanglement swapping of multiple orbital angular momentum states of light, Nature Communications **8**, 10.1038/s41467-017-00706-1 (2017).

[20] S. Takeda, M. Fuwa, P. van Loock, and A. Furusawa, Entanglement swapping between discrete and continuous variables, Physical Review Letters **114**, 100501 (2015).

[21] A. K. Jha, G. S. Agarwal, and R. W. Boyd, Supersensitive measurement of angular displacements using entangled photons, Physical Review A **83**, 053829 (2011).

[22] L. Chen, J. Lei, and J. Romero, Quantum digital spiral imaging, Light: Science & Applications **3**, e153 (2014).

[23] S. Asban, K. E. Dorfman, and S. Mukamel, Quantum phase-sensitive diffraction and imaging using entangled photons, Proceedings of the National Academy of Sciences , 201904839 (2019).

[24] L. Neves, G. Lima, J. G. A. Gómez, C. H. Monken, C. Saavedra, and S. Pádua, Generation of entangled states of qudits using twin photons, Physical Review Letters **94**, 100501 (2005).

[25] A. Mair, A. Vaziri, G. Weihs, and A. Zeilinger, Entanglement of the orbital angular momentum states of photons, Nature **412**, 313 (2001).

[26] C. K. Law and J. H. Eberly, Analysis and interpretation of high transverse entanglement in optical parametric down conversion, Physical Review Letters **92**, 127903 (2004).

[27] C. H. Bennett, G. Brassard, C. Crépeau, R. Jozsa, A. Peres, and W. K. Wootters, Teleporting an unknown quantum state via dual classical and einstein-podolsky-rosen channels, Physical

Review Letters **70**, 1895 (1993).

[28] A. K. Ekert, Quantum cryptography based on bell's theorem, Physical Review Letters **67**, 661 (1991).

[29] F. Bouchard, K. Heshami, D. England, R. Fickler, R. W. Boyd, B.-G. Englert, L. L. Sánchez-Soto, and E. Karimi, Experimental investigation of high-dimensional quantum key distribution protocols with twisted photons, Quantum **2**, 111 (2018).

[30] Y. Ding, D. Bacco, K. Dalgaard, X. Cai, X. Zhou, K. Rottwitt, and L. K. Oxenløwe, High-dimensional quantum key distribution based on multicore fiber using silicon photonic integrated circuits, npj Quantum Information **3**, 10.1038/s41534-017-0026-2 (2017).

[31] A. Vaziri, J.-W. Pan, T. Jennewein, G. Weihs, and A. Zeilinger, Concentration of higher dimensional entanglement: Qutrits of photon orbital angular momentum, Physical Review Letters **91**, 227902 (2003).

[32] G. A. Tyler, Spatial bandwidth considerations for optical communication through a free space propagation link, Optics Letters **36**, 4650 (2011).

[33] J. Zhao, M. Mirhosseini, B. Braverman, Y. Zhou, S. M. H. Rafsanjani, Y. Ren, N. K. Steinhoff, G. A. Tyler, A. E. Willner, and R. W. Boyd, Performance analysis of d -dimensional quantum cryptography under state-dependent diffraction, Physical Review A **100**, 032319 (2019).

[34] J. Romero, D. Giovannini, S. Franke-Arnold, S. M. Barnett, and M. J. Padgett, Increasing the dimension in high-dimensional two-photon orbital angular momentum entanglement, Physical Review A **86**, 012334 (2012).

[35] H. D. L. Pires, H. C. B. Florijn, and M. P. van Exter, Measurement of the spiral spectrum of entangled two-photon states, Physical Review Letters **104**, 020505 (2010).

[36] G. Kulkarni, L. Taneja, S. Aarav, and A. K. Jha, Angular schmidt spectrum of entangled photons: Derivation of an exact formula and experimental characterization for noncollinear phase matching, Physical Review A **97**, 063846 (2018).

[37] J. P. Torres, A. Alexandrescu, and L. Torner, Quantum spiral bandwidth of entangled two-photon states, Physical Review A **68**, 050301 (2003).

[38] F. M. Miatto, A. M. Yao, and S. M. Barnett, Full characterization of the quantum spiral bandwidth of entangled biphotons, Physical Review A **83**, 033816 (2011).

[39] S. Liu, Y. Zhang, C. Yang, S. Liu, Z. Ge, Y. Li, Y. Li, Z. Zhou, G. Guo, and B. Shi, Increasing two-photon entangled dimensions by shaping input-beam profiles, Physical Review A **101**,

052324 (2020).

[40] S. Liu, Z. Zhou, S. Liu, Y. Li, Y. Li, C. Yang, Z. Xu, Z. Liu, G. Guo, and B. Shi, Coherent manipulation of a three-dimensional maximally entangled state, Physical Review A **98**, 062316 (2018).

[41] E. V. Kovlakov, S. S. Straupe, and S. P. Kulik, Quantum state engineering with twisted photons via adaptive shaping of the pump beam, Physical Review A **98**, 060301 (2018).

[42] S. Karan, S. Aarav, H. Bharadhwaj, L. Taneja, A. De, G. Kulkarni, N. Meher, and A. K. Jha, Phase matching in β-barium borate crystals for spontaneous parametric down-conversion, Journal of Optics **22**, 083501 (2020).

[43] S. Walborn, C. Monken, S. Pádua, and P. S. Ribeiro, Spatial correlations in parametric down-conversion, Physics Reports **495**, 87 (2010).

[44] C. K. Hong and L. Mandel, Theory of parametric frequency down conversion of light, Physical Review A **31**, 2409 (1985).

[45] A. M. Yao, Angular momentum decomposition of entangled photons with an arbitrary pump, New Journal of Physics **13**, 053048 (2011).

[46] A. Cerjan and C. Cerjan, Orbital angular momentum of laguerre–gaussian beams beyond the paraxial approximation, Journal of the Optical Society of America A **28**, 2253 (2011).

[47] J. Chani-Cahuana, C. Fager, and T. Eriksson, Lower bound for the normalized mean square error in power amplifier linearization, IEEE Microwave and Wireless Components Letters **28**, 425 (2018).

[48] M. R. Bonyadi and Z. Michalewicz, Particle swarm optimization for single objective continuous space problems: A review, Evolutionary Computation **25**, 1 (2017).

[49] G. Kulkarni, R. Sahu, O. S. Magaña-Loaiza, R. W. Boyd, and A. K. Jha, Single-shot measurement of the orbital-angular-momentum spectrum of light, Nature Communications **8**, 10.1038/s41467-017-01215-x (2017).

[50] V. Arrizón, U. Ruiz, R. Carrada, and L. A. González, Pixelated phase computer holograms for the accurate encoding of scalar complex fields, Journal of the Optical Society of America A **24**, 3500 (2007).

[51] A. Ekert and P. L. Knight, Entangled quantum systems and the schmidt decomposition, American Journal of Physics **63**, 415 (1995).

[52] A. K. Jha, G. S. Agarwal, and R. W. Boyd, Partial angular coherence and the angular schmidt spectrum of entangled two-photon fields, Physical Review A **84**, 063847 (2011).

Postselection-free controlled generation of high-dimensional OAM entangled state: Supplementary Information

Suman Karan,* Radhika Prasad, and Anand K. Jha

Department of Physics, Indian Institute of Technology Kanpur, Kanpur, UP 208016, India

arXiv:2203.14799v1 [quant-ph] 28 Mar 2022

I. CALCULATION OF PHASE MISMATCH PARAMETER

Spontaneous parametric down-conversion process (SPDC) is a second-order nonlinear optical process, in which a pump (p) photon of higher frequency passes through a nonlinear crystal and is down-converted into two lower-frequency photons called signal (s) and idler (i).The phase matching function as given in Eq. (10) of the manuscript is

$$\Phi(\rho_s, \rho_i, \phi_s, \phi_i) = \text{sinc}\left(\frac{\Delta k_z L}{2}\right) \exp\left[i\frac{\Delta k_z L}{2}\right]. \tag{1}$$

Here L is the thickness of the crystal and Δk_z is called the phase mismatch parameter and is given by

$$\Delta k_z = k_{sz} + k_{iz} - k_{pz}, \tag{2}$$

where k_{sz}, k_{iz} and k_{pz} represent the longitudinal wave vector components along z-direction for signal, idler and pump fields. For the type-I SPDC process, the pump polarization is extraordinary, whereas the polarizations of the signal and idler photons are ordinary. Therefore, we write k_{jz} with $j = p, s, i$ as [1]

$$\begin{aligned}
k_{pz} &= -\alpha_p q_{px} + \eta_p K_{p0} - \frac{\left[\beta_p^2 q_{px}^2 + \gamma_p^2 q_{py}^2\right]}{2\eta_p K_{p0}}, \\
k_{sz} &= n_{so} K_{s0} - \frac{1}{2n_{so}K_{s0}}(q_{sx}^2 + q_{sy}^2), \\
k_{iz} &= n_{io} K_{i0} - \frac{1}{2n_{io}K_{i0}}(q_{ix}^2 + q_{iy}^2),
\end{aligned}$$

where $K_{j0} = \frac{2\pi}{\lambda_j}$ with λ_j being the wavelength and n_{jo} and n_{je} being the refractive index for ordinary and extraordinary polarizations. The quantities α_p , β_p, γ_p and η_p are given by

$$\begin{aligned}
\alpha_p &= \frac{(n_{po}^2 - n_{pe}^2)\sin\theta_p \cos\theta_p}{n_{po}^2 \sin^2\theta_p + n_{pe}^2 \cos^2\theta_p}, \\
\beta_p &= \frac{n_{po} n_{pe}}{n_{po}^2 \sin^2\theta_p + n_{pe}^2 \cos^2\theta_p}, \\
\gamma_p &= \frac{n_{po}}{\sqrt{n_{po}^2 \sin^2\theta_p + n_{pe}^2 \cos^2\theta_p}}, \\
\eta_p &= \frac{n_{po} n_{pe}}{\sqrt{n_{op}^2 \sin^2\theta_p + n_{pe}^2 \cos^2\theta_p}},
\end{aligned}$$

* sumankaran2@gmail.com

where θ_p is the phase matching angle. In our experiment, we use β-barium borate (BBO) crystal for down-conversion, and for that, the values of n_{po}, n_{pe} can be obtained from the dispersion relation reported in Ref. [2].

In the case of degenerate SPDC process, signal and idler have the same frequency. Therefore, we can write $K_{s0} \approx K_{i0} \approx K_{p0}/2$ and $n_{so} = n_{io}$. Numerically, we find that for our experimental parameters, $\alpha_p \approx 0$ and $\beta_p \approx \gamma_p \approx 1$. Thus, Δk_z of Eq. (2) can be written in transverse momentum basis as

$$\Delta k_z = K_{p0}\left[n_{so} - \eta_p\right] - \frac{1}{2\eta_p K_{p0}}\left[\rho_s^2 + \rho_i^2 - 2\rho_s\rho_i\, \boldsymbol{c}os\left(\phi_s - \phi_i\right)\right]. \tag{3}$$

II. SUPERPOSITION COEFFICIENTS

Table I presents the complex coefficients α_p for generating pump field superposition of five radial modes having $p = 0$ to $p = 4$ for generating three separate OAM Schmidt spectra as shown in Fig. 3 in the main text. Table II presents the complex coefficients α_p for generating pump field superposition of five radial modes having $p = 0$ to $p = 4$ for generating three separate OAM Schmidt spectra as shown in Fig. 4 in the main text. For both Table I and II, the width of the Gaussian spectrum is characterized by the standard deviation. We take the width of the rectangular spectrum to be the size of the rectangle and that of the triangular spectrum to be the width of the base.

TABLE I. Superposition coefficients (α_p) for experimentally generated OAM Schmidt spectra reported in Fig. 3 in the main text

Spectrum	Width	Complex coefficients				
		α_0	α_1	α_2	α_3	α_4
Gaussian	20	$-0.68 - 0.68i$	$0.14 + 0.01i$	$0.00 + 0.00i$	$0.24 + 0.00i$	$0.00 + 0.00i$
	30	$-0.56 - 0.56i$	$0.31 - 0.31i$	$0.00 + 0.00i$	$0.44 + 0.00i$	$0.01 + 0.00i$
rectangular	100	$0.23 + 0.11i$	$-0.56 - 0.09i$	$-0.23 - 0.05i$	$0.18 - 0.07i$	$0.25 - 0.68i$
	150	$0.14 + 0.00i$	$-0.39 + 0.04i$	$0.71 - 0.32i$	$-0.28 + 0.21i$	$0.14 + 0.28i$
triangular	100	$-0.93 - 0.09i$	$-0.13 + 0.00i$	$0.22 - 0.13i$	$-0.20 + 0.01i$	$0.00 + 0.00i$
	200	$0.04 + 0.34i$	$-0.55 - 0.04i$	$0.42 - 0.13i$	$-0.04 - 0.46i$	$0.00 + 0.42i$

TABLE II. Superposition coefficients (α_p) for experimentally generated OAM Schmidt spectra reported in Fig. 4 in the main text

Spectrum	Width	Complex coefficients				
		α_0	α_1	α_2	α_3	α_4
Gaussian	20	$-0.17+0.82i$	$0.34-0.03i$	$0.34-0.03i$	$-0.17+0.00i$	$-0.20+0.03i$
	30	$-0.78+0.43i$	$0.31-0.03i$	$0.25-0.03i$	$-0.17+0.00i$	$-0.14+0.03i$
rectangular	100	$0.83+0.00i$	$0.31+0.18i$	$-0.14+0.13i$	$0.00+0.35i$	$0.00+0.18i$
	150	$0.20+0.20i$	$-0.83+0.00i$	$0.22-0.23i$	$0.10-0.33i$	$-0.10-0.02i$
triangular	100	$0.19+0.97i$	$0.02+0.01i$	$-0.09-0.09i$	$0.06+0.06i$	$-0.01+0.02i$
	200	$0.03+0.32i$	$-0.87-0.03i$	$0.03-0.15i$	$-0.15-0.26i$	$0.00+0.15i$

[1] S. Karan, S. Aarav, H. Bharadhwaj, L. Taneja, A. De, G. Kulkarni, N. Meher, and A. K. Jha, Phase matching in β-barium borate crystals for spontaneous parametric down-conversion, Journal of Optics **22**, 083501 (2020).

[2] D. Eimerl, L. Davis, S. Velsko, E. K. Graham, and A. Zalkin, Optical, mechanical, and thermal properties of barium borate, Journal of Applied Physics **62**, 1968 (1987).